Journal of Physics and Chemistry of Solids 69 (2008) 2146–2150

Contents lists available at ScienceDirect

Journal of Physics and Chemistry of Solids

journal homepage: www.elsevier.com/locate/jpcs

Structure of $CaMnO_3$ in the range $10\,K \leqslant T \leqslant 550\,K$ from neutron time-of-flight total scattering

E.S. Božin [a,*], A. Sartbaeva [b], H. Zheng [c], S.A. Wells [b], J.F. Mitchell [c], Th. Proffen [d], M.F. Thorpe [b], S.J.L. Billinge [a]

[a] Department of Physics and Astronomy, Michigan State University, 4250 Biomedical Physical Sciences, East Lansing, MI 48824-2320, USA
[b] Department of Physics, Arizona State University, Tempe, AZ 85283, USA
[c] Material Science Division, Argonne National Laboratory, Argonne, IL 60439, USA
[d] Los Alamos National Laboratory, LANSCE-LC, MS H805, Los Alamos, NM 87545, USA

ARTICLE INFO

Keywords:
A. Oxides
C. Neutron scattering
D. Crystal structure

ABSTRACT

The local and average structure of the Ca endmember of the $La_{1-x}Ca_xMnO_3$ series has been investigated. Neutron powder diffraction-based high real-space resolution atomic pair distribution function (PDF) analysis, yielding the local atomic structure, and the corresponding Rietveld analysis yielding the average crystal structure show that the two structural scales are in accord in this material, and that the MnO_6 octahedral units are regular for all temperatures studied. Quantitative values of structural parameters are reported for a wide temperature range, important for both experimental and theoretical considerations of hole and electron doped branches of the rich phase diagram of $La_{1-x}Ca_xMnO_3$.

1. Introduction

Colossal responses, such as high-temperature superconductivity, colossal magnetoresistance (CMR) and ferroelectricity, have brought doped transition metal oxides into focus during the past two decades [1]. This is not only due to their importance for potential applications, but also as these materials represent an extremely fertile ground for verification of various fundamental physical concepts.

The manganite-based perovskite $La_{1-x}Ca_xMnO_3$ family in particular has been the subject of enhanced interest as it exhibits a complex interplay of orbital, electronic, and magnetic degrees of freedom [2]. This system is of great value to the oxide community as it is dopable over the full range of Ca concentrations between 0 and 1. The appearance of the insulator-to-metal phase transition and the CMR effect for Ca-doping between 0.2 and 0.5 are certainly among the most prominent features, whose mechanisms are still not fully understood. The importance of the atomic structure to understand the CMR properties of manganites, especially that on a nanometer lengthscale, has been established [3,4]. However, the lack of complete understanding of the exact role that local structure plays extends to the present time [5,6]. Knowledge of accurate values of the structural parameters of the La and Ca endmembers over a broad temperature range is essential both for numerical studies [7] and for experimental considerations such as those aimed to quantify the phase fractions as part of an effort to verify (or otherwise) the phase separation scenario [8]. While the rich structure of the La endmember has been studied in detail over an extremely wide temperature range [2,9–11], the structure of the Ca endmember has been quantified less extensively and for fewer temperatures [12].

In this paper we report the results of a neutron total scattering experiment on $CaMnO_3$ over a wide temperature range, bridging the gap and complementing the detailed structural work carried out over the same temperature range for a dense series of Ca concentrations in the hole-doped branch of the phase diagram [6]. This provides important (and so far missing) experimental information allowing for the quantification of microscopic phase separation in $La_{1-x}Ca_xMnO_3$, among other things.

2. Experimental

Powder $CaMnO_3$ sample was synthesized using standard solid state reaction from high purity $CaCO_3$ and MnO_2 starting materials. The mixed powder was ground and fired in air at 900, 1000, and 1050 °C, successively, with intermediate grindings. Finally, the powder was pressed into a pellet and fired at 1070 °C. The as-made pellet was annealed at 500 °C, under 2650 psi O_2 pressure, with 0.1 C/min cooling rate to room temperature. The final high pressure treatment was necessary to suppress the occurrence of the Marokite impurity phase and to optimize

---

[*] Corresponding author. Tel.: +1 517 355 9200; fax: +1 517 353 4500.
E-mail address: bozin@pa.msu.edu (E.S. Božin).

0022-3697/$ - see front matter © 2008 Elsevier Ltd. All rights reserved.
doi:10.1016/j.jpcs.2008.03.029

the oxygen stoichiometry. The crystallographic behavior was confirmed by means of X-ray diffraction characterization.

Time-of-flight (TOF) neutron diffraction measurements were carried out on the NPDF diffractometer at LANSCE at Los Alamos National Laboratory. The local structural information is accessed by means of the real-space atomic pair distribution function (PDF) analysis of the neutron diffraction data collected at seven temperatures from 10 K up to 550 K. Approximately 5 g of finely pulverized sample was sealed in an extruded cylindrical vanadium tube with He exchange gas. The sample was cooled using a closed-cycle He refrigerator. The data were corrected for experimental effects and normalized [13] to obtain the total scattering function $S(Q)$ [14], where $Q=|\mathbf{Q}|=|\mathbf{k}-\mathbf{k}_0|$ represents the momentum transfer magnitude for the scattering. The PDF function, $G(r)$, is then obtained by a Fourier transformation according to

$$G(r)=\frac{2}{\pi}\int_0^\infty Q[S(Q)-1]\sin(Qr)\,dQ. \tag{1}$$

A typical total scattering structure function, $F(Q)$, and the corresponding PDF, $G(r)$, are shown in Fig. 1. The function $G(r)$ gives the probability of finding an atom at a distance r from another atom. This function is obtained directly from the Fourier transform of the neutron diffraction data and is used to investigate features of the *local* structure of a material. The radial distribution function (RDF), $R(r)$, relates to $G(r)$ through a series of simple arithmetic operations [13]. Both $G(r)$ and $R(r)$ functions are peaked at distances separating pairs of atoms. The PDFs presented here used high resolution total scattering data up to a very high value of momentum transfer ($Q_{MAX}=35\,\text{Å}^{-1}$) and were reduced from the raw data using the PDFgetN program package [15].

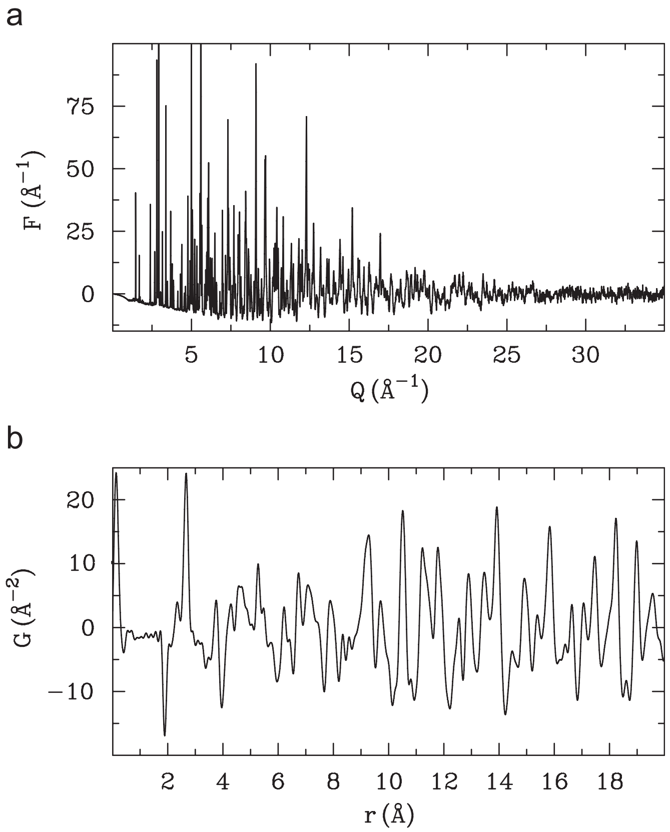

Fig. 1. Reduced total scattering structure function, $F(Q)=Q(S(Q)-1)$, of $CaMnO_3$ at 10 K (a) and corresponding atomic pair distribution function, $G(r)$, (b) obtained through a Fourier transform. Upper limit of integration in the transform, Q_{max}, was set to 35 Å^{-1}.

3. Modeling

Structural modeling was carried out in reciprocal and in direct space. The Rietveld refinements were done using the GSAS program [16] controlled by EXPGUI [17]. Structural refinements in direct space were performed using the PDFfit2 modeling engine controlled by PDFgui [18]. The PDF modeling was carried out over a 19.5 Å r-range using the constraints of the orthorhombic Pnma space group, with 16 parameters refined. These are three lattice parameters and seven fractional coordinates as permitted by symmetry, four isotropic atomic displacement parameters (ADPs), correlated motion parameter δ_2 associated with the quadratic term [13], and a scale factor. The Rietveld refinements were done with the same set of parameters, except for the one pertaining to the correlated motion, and in addition six background parameters using GSAS background function 4 (expansion of the exponential), and two peak profile parameters. Very good fits were obtained for all the data sets. Example refinements are shown in Fig. 2: Rietveld fits for 425 and 130 K data are presented in Fig. 2(a) and (b), respectively, while the PDF fits of the data at the same two temperatures are shown in panels (c) and (d), respectively.

We have recently [19] investigated the structure of $LaMnO_3$ by fitting large structural models to PDF data, using simulated-annealing combined with geometric constraints [20], which allows for the presence or absence of Jahn–Teller (JT) distortions in the MnO_6 octahedra to be studied. Here we apply the same approach to $CaMnO_3$. For each temperature point our starting model was a $16\times16\times12$ supercell of the PDF-refined crystal structure, with cell edges of about 90 Å, containing 61 440 atoms (12 288 octahedra). This starting structure was refined following

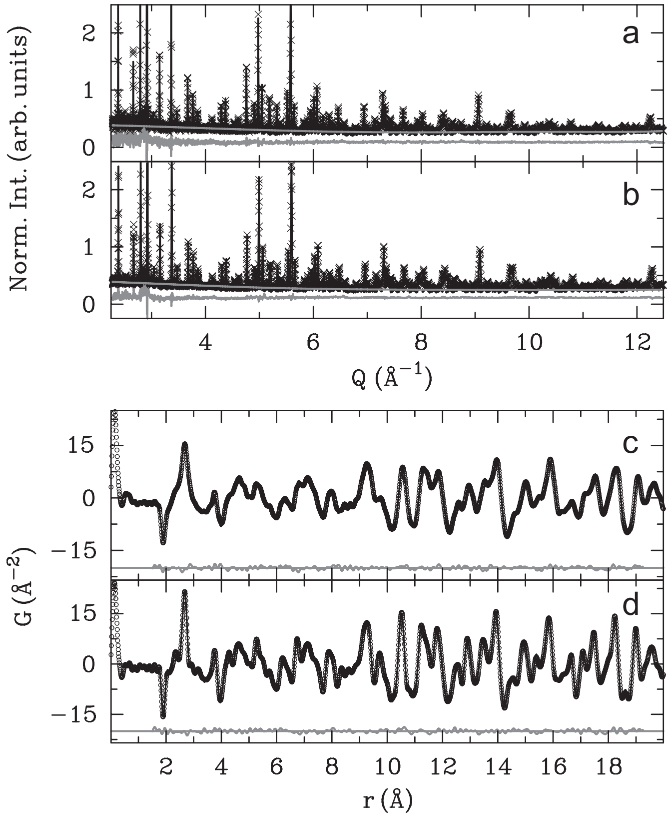

Fig. 2. Typical orthorhombic model refinements of the total scattering data. (a) 425 K and (b) 130 K Rietveld refinements. (c) 425 K and (d) 130 K PDFfit refinements. In all cases, symbols are the data, solid line is the refined profile, and the offset gray line is the difference curve. The gray line in the Rietveld plots underneath the data is the calculated background function.

the procedure described in Ref. [19]. Such large models can give unphysical results [21] and constraints must be used to ensure that local chemical bonding and steric exclusion are properly maintained. Our geometrically constrained refinement approach constrains the bonding geometry of the MnO_6 octahedra using a system of geometric templates [20,22,23] which allow each octahedron to adopt either regular or JT distorted geometry, as described in more detail in Ref. [19]. From the fully converged models we obtained the distribution of quadrupole distortions of the octahedra to look for evidence in the data for the existence of JT distortions. The five components of a quadrupole q are defined in terms of the components x, y, z of the six MnO bond vectors in each octahedron, as follows:

$$q_1 = 2\sum_{i=1}^{6} x_i y_i, \quad q_2 = 2\sum_{i=1}^{6} y_i z_i,$$
$$q_3 = 2\sum_{i=1}^{6} z_i x_i, \quad q_4 = \sum_{i=1}^{6} (x_i^2 - y_i^2),$$
$$q_5 = \frac{1}{\sqrt{3}}\sum_{i=1}^{6} (2z_i^2 - x_i^2 - y_i^2). \tag{2}$$

4. Results and discussion

The results of the refinements for all temperatures are reported in Table 1. Excellent agreement is observed between the PDF and Rietveld refined parameters, confirming that there are no significant local structural distortions in this material, as expected. The refined fractional coordinates are largely within the estimated uncertainties, which gives confidence in their accuracy given that they are being refined using different techniques. The ADPs are consistently lower in the PDF refinements. We might expect that the PDF data give more accurate ADPs because the data-range that is probed is wider and the refined ADPs are not correlated with a fitted background function. The fact that they are so small in the PDF refinements is a good indicator that there is little in the way of local structural disorder in this material. The refined lattice parameters are close between the PDF and Rietveld refinements, but are consistently overestimated by $\sim$0.004 A in the PDF results. This is a known problem with PDF data derived from TOF neutron data that has asymmetric diffraction peak profiles [24] and this aberration has not been corrected in the current fits, so the Rietveld refined lattice parameters should be considered as the accurate values.

A parameter of interest in the manganites is the MnO bond-length, which is highly sensitive to the electronic state of the manganese [3,6]. In Table 2 we reproduce the values of this bond-length determined from the Rietveld refinements. The peaks corresponding to the nearest neighbor MnO correlations appear negative due to negative neutron scattering length of manganese. The presence of the JT distortion is clearly apparent in the $LaMnO_3$ data with a broad peak from the four shorter bonds centered around 1.92 Å and a completely resolved peak at 2.16 Å coming from the two long bonds. In the case of $CaMnO_3$ the peak has clearly collapsed to a single Gaussian and shifted to shorter-r. This shows that the octahedra have become regular in the Mn^{4+} case, with an average bond length that is shorter than the short-bonds of the Mn^{3+} in $LaMnO_3$. This is expected as Mn^{4+} in a cubic crystal field is not a JT ion [1]. This is reflected in the refined bond-lengths shown in Table 2.

The length of the longer MnO bonds is seen to decrease continuously with Ca doping [6]. In a charge-segregated model this behavior is expected to occur in the average bond-length, but not the bond-length determined locally, for example, from the PDF. The current result gives us a well-defined endmember value against which to compare the doping dependent behavior in $La_{1-x}Ca_xMnO_3$. The model was orthorhombic, allowing for three independent bond-lengths. However, all three values refined to approximately the same length of roughly 1.90 Å. This is slightly shorter than the average of the "short" MnO bonds in the MnO_6 octahedra of $LaMnO_3$ where the Mn is in the 3+ state. These bonds are 1.92 and 1.97 Å, respectively, at 20 K [10] giving an average value of 1.945 Å. This compares with the average MnO bond-length of 1.90 Å at 10 K in $CaMnO_3$ found here. The unstrained MnO_6 octahedra for Mn^{4+} charge-state are therefore smaller. If, in the doped systems, holes localize to make locally 4+ sites in a background of 3+ ions, this will result in a local strain.

It is interesting to compare the nature of the PDF in the region of the first few coordination shells to see the effect on the PDF of changing the shape of the MnO_6 octahedron as we go from Mn^{3+} to Mn^{4+}. Fig. 3 shows a comparison of the low-r region of the RDFs, $R(r)$, for $LaMnO_3$ (gray profile) and $CaMnO_3$ (black profile) at 10 K temperature.

Table 1
PDF and Rietveld refinement results for $CaMnO_3$

T (K)	Rietveld					PDF				
	10	130	300	425	550	10	130	300	425	550
a (Å)	5.2757(1)	5.2782(1)	5.2816(1)	5.2850(1)	5.2884(1)	5.2790(2)	5.2808(2)	5.2834(3)	5.2856(10)	5.2917(6)
b (Å)	7.4398(1)	7.4435(1)	7.4567(1)	7.4666(2)	7.4761(2)	7.4438(3)	7.4482(3)	7.4624(5)	7.4781(13)	7.4803(8)
c (Å)	5.2555(1)	5.2577(1)	5.2671(1)	5.2748(1)	5.2820(1)	5.2583(2)	5.2609(2)	5.2716(3)	5.2756(8)	5.2870(4)
Ca x	0.0348(2)	0.0348(2)	0.0327(2)	0.0310(3)	0.0293(3)	0.0342(1)	0.0344(1)	0.0331(1)	0.0310(3)	0.0294(2)
Ca z	0.9936(4)	0.9939(4)	0.9946(4)	0.9943(7)	0.9945(6)	0.9935(1)	0.9931(1)	0.9944(2)	0.9918(6)	0.9922(3)
O1 x	0.4896(2)	0.4894(2)	0.4901(2)	0.4906(4)	0.4910(4)	0.4883(1)	0.4877(1)	0.4879(1)	0.4871(3)	0.4865(2)
O1 z	0.0674(3)	0.0671(2)	0.0661(3)	0.0658(4)	0.0653(4)	0.0673(1)	0.0671(1)	0.0649(2)	0.0669(4)	0.0644(2)
O2 x	0.2867(2)	0.2875(1)	0.2872(2)	0.2869(2)	0.2863(2)	0.2870(1)	0.2873(1)	0.2876(1)	0.2862(3)	0.2867(2)
O2 y	0.0347(1)	0.0342(1)	0.0337(1)	0.0328(2)	0.0321(1)	0.0345(1)	0.0346(1)	0.0342(1)	0.0323(2)	0.0313(1)
O2 z	0.7122(2)	0.7115(1)	0.7120(2)	0.7125(2)	0.7133(2)	0.7116(1)	0.7109(1)	0.7109(1)	0.7120(3)	0.7120(2)
Ca U_{iso} (Å^2)	0.0042(2)	0.0047(1)	0.0078(2)	0.0098(3)	0.0118(3)	0.0030(1)	0.0036(1)	0.0058(1)	0.0081(2)	0.0095(2)
Mn U_{iso} (Å^2)	0.0028(2)	0.0029(1)	0.0043(1)	0.0052(2)	0.0059(2)	0.0017(1)	0.0022(1)	0.0034(1)	0.0035(2)	0.0049(1)
O1 U_{iso} (Å^2)	0.0044(2)	0.0048(1)	0.0070(2)	0.0083(2)	0.0102(2)	0.0036(1)	0.0039(1)	0.0057(1)	0.0063(2)	0.0073(1)
O2 U_{iso} (Å^2)	0.0047(1)	0.0050(1)	0.0073(1)	0.0091(2)	0.0108(2)	0.0037(1)	0.0043(1)	0.0065(1)	0.0085(1)	0.0100(1)
R_w	0.038	0.034	0.042	0.072	0.085	0.094	0.073	0.077	0.126	0.084

All refinements were carried out using a structural model with orthorhombic symmetry (space group Pnma), with O1 occupying 4c $(x, 0.25, z)$, and O2 occupying 8d (x, y, z) positions. Ca was at $(x, 0.25, x)$ and Mn at (0.5,0.0,0.0) site.

Table 2
MnO distances and Mn–O2–Mn angles for $10\,\mathrm{K} \leqslant T \leqslant 550\,\mathrm{K}$ temperature range obtained from the Rietveld refinements

T (K)	$r(\mathrm{MnO})_{short}$ (Å)	$r(\mathrm{MnO})_{medium}$ (Å)	$r(\mathrm{MnO})_{long}$ (Å)	θ(Mn–O2–Mn) (deg)
10	1.89421(28)	1.8971(9)	1.9026(9)	156.98(5)
70	1.89454(27)	1.8976(8)	1.9027(8)	156.94(5)
130	1.89485(24)	1.8985(8)	1.9036(8)	156.89(4)
190	1.89563(23)	1.9000(7)	1.9034(8)	156.89(4)
250	1.89661(25)	1.8995(8)	1.9045(8)	157.05(5)
300	1.89715(25)	1.9003(8)	1.9045(8)	157.18(5)
425	1.89920(40)	1.9013(14)	1.9050(14)	157.55(7)
550	1.90120(40)	1.9025(14)	1.9047(14)	158.00(7)

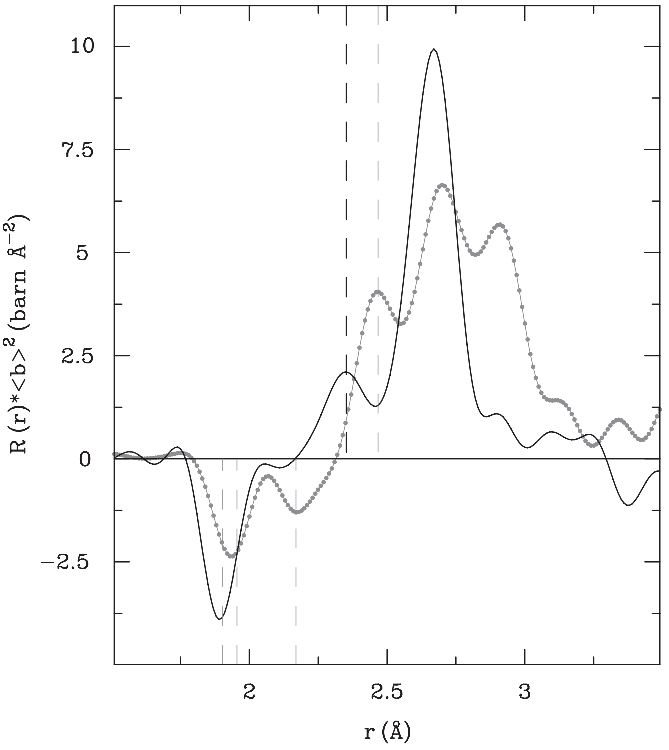

Fig. 3. Comparison of the radial distribution function, $R(r)$, for $\mathrm{CaMnO_3}$ (solid black line) and $\mathrm{LaMnO_3}$ (dotted gray line) at 10 K temperature. The figure shows the RDF peaks that describe the $\mathrm{MnO_6}$ octahedron. The set of negative peaks at around 2 and 2.17 Å belong to the MnO bonds constituting the octahedron. The peaks are negative due to the negative neutron scattering length of Mn. Vertical dashed lines below $r = 2.25$ A denote the positions of the MnO distances refined from $\mathrm{LaMnO_3}$. The two vertical dashed lines above $r = 2.25$ A mark the position of the nearest LaO and CaO distances in the structures of the La and Ca endmembers, respectively.

Significant changes are also seen in the 2.75 and 2.85 Å oxygen–oxygen correlations that appear as a single peak in the $\mathrm{CaMnO_3}$ data but are split into a multiplet in the JT distorted $\mathrm{LaMnO_3}$ case. It is also worth noticing that the LaO peak at ~2.48 A shifts considerably, becoming a CaO peak centered at ~2.36 A for the Ca endmember. This is expected based on the relative size of La and Ca [25]. The intensity of the LaO RDF peak is twice that of the CaO peak due to the fact that the scattering length of La is nearly twice that of Ca, and the RDF peak intensity is scaled with the scattering lengths of the contributing atomic pairs.

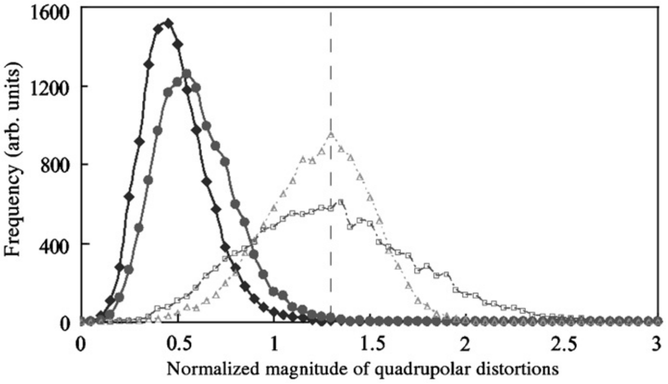

Fig. 4. Distribution of magnitudes of quadrupole distortions for the octahedra in large models of $\mathrm{LaMnO_3}$ at 300 K (open, dashed, triangles) and 1050 K (open, dashed, squares), and for $\mathrm{CaMnO_3}$ at 130 K (closed, solid, rhombus) and 425 K (closed, solid, circles). The magnitudes are normalized and dimensionless such that an octahedron with two long bonds of 2.16 Å and four short bonds of 1.94 Å would have a distortion of 1. In $\mathrm{LaMnO_3}$ both distributions peak at around 1.3, indicating a strong JT distortion, and the width increases with temperature. In $\mathrm{CaMnO_3}$, the distortions are much smaller and the peak positions increase slightly with temperature. This is consistent with the distortions in the $\mathrm{CaMnO_3}$ models being due to thermal variations in atomic positions, with no systematic JT distortion. The dashed line indicates the position of average quadrupole distributions for $\mathrm{LaMnO_3}$ at 1.3, which does not move with temperature.

The octahedra in the average crystal structure are regular and have no significant quadrupole distortions. In the case of $\mathrm{LaMnO_3}$, there is a discrepancy at high temperatures between the average and local structures [11]. In our large models refined using geometrically constrained refinement [19] we observed large quadrupoles on all octahedra due to the persistence of the JT distortion. The distribution of quadrupole distortions in $\mathrm{LaMnO_3}$ displayed a peak at a large value appropriate to the fully JT-distorted octahedron seen in the low-temperature crystal structure. The width of the distribution increased with temperature, but the position of the peak did not move. However, in $\mathrm{CaMnO_3}$ we find the distribution of quadrupole distortion peaks at a much lower value, as shown in Fig. 4. Both the peak position and the width of the distribution increase with temperature. Thermal variations in atomic positions produce small quadrupolar distortions of octahedra. From the width of the thermal variation in MnO bond lengths, we can estimate the average magnitude of these small distortions. The FWHM of the distributions of MnO bond lengths are approximately 0.11 Å at 130 K and 0.16 Å at 425 K. From Eq. (2) this gives an average quadrupole of ~0.3 at 130 K and 0.5 at 425 K, consistent with our refined results (Fig. 4). The geometrically constrained refinement [19] therefore supports structural results that show, for example, at 130 K a small static distortion of ~0.009 A coupled with thermal motion amplitude of ~0.08 A.

5. Summary

In summary, structural parameters for $\mathrm{CaMnO_3}$, in the Pnma space group, over the $10\,\mathrm{K} \leqslant T \leqslant 550\,\mathrm{K}$ temperature range are presented, as obtained from neutron time-of-flight total scattering experiments. Results of Rietveld and PDF analyses are in accord, showing that the $\mathrm{MnO_6}$ octahedral units are regular across the temperature range studied. The evolution of the MnO bond lengths is discussed as the sample goes from pure $\mathrm{Mn^{3+}}$ in $\mathrm{LaMnO_3}$ to $\mathrm{Mn^{4+}}$ in $\mathrm{CaMnO_3}$.

Acknowledgments

Work at MSU and ASU was supported by the NSF under Grant no. DMR-0304391. Work at Argonne National Laboratory is supported under Contract no. DE-AC02-06CH1137. Beamtime on NPDF at Lujan Center at Los Alamos National Laboratory was funded under DOE Contract no. DEAC52-06NA25396. Simulations were run on the Saguaro High-Performance Computing Facility at ASU.

References

[1] A.J. Millis, Lattice effects in magnetoresistive manganese perovskites, Nature 392 (1998) 147.

[2] E.O. Wollan, W.C. Koehler, Neutron-diffraction study of the magnetic properties of the series of perovskite-type compounds La_{1-x},Ca_xMnO_3, Phys. Rev. 100 (1955) 545–563.

[3] S.J.L. Billinge, R.G. DiFrancesco, G.H. Kwei, J.J. Neumeier, J.D. Thompson, Direct observation of lattice polaron formation in the local structure of La_{1-x},Ca_xMnO_3, Phys. Rev. Lett. 77 (1996) 715–718.

[4] C.H. Booth, F. Bridges, G.H. Kwei, J.M. Lawrence, A.L. Cornelius, J.J. Neumeier, Direct relationship between magnetism and MnO_6 distortions in La_{1-x},Ca_xMnO_3, Phys. Rev. Lett. 80 (4) (1998) 853–856.

[5] E.S. Božin, X. Qiu, M. Schmidt, G. Paglia, J.F. Mitchell, P.G. Radaelli, Th. Proffen, S.J.L. Billinge, Local structural aspects of the orthorhombic to pseudo-cubic phase transformation in $La_{1-x}Ca_xMnO_3$, Physica B 385–386 (2006) 110–112.

[6] E.S. Božin, M. Schmidt, A.J. DeConinck, G. Paglia, J.F. Mitchell, T. Chatterji, P.G. Radaelli, Th. Proffen, S.J.L. Billinge, Understanding the insulating phase in CMR manganites: shortening of the Jahn–Teller long-bond across the phase diagram of $La_{1-x}Ca_xMnO_3$, Phys. Rev. Lett. 98 (2007) 137203.

[7] E. Dagotto, Complexity in strongly correlated electronic systems, Science 309 (2005) 257–262.

[8] Th. Proffen, S.J.L. Billinge, Probing the local structure of doped manganites using the atomic pair distribution function, Appl. Phys. A 74 (2002) 1770.

[9] J. Rodriguez-Carvajal, M. Hennion, F. Moussa, A.H. Moudden, L. Pinsard, A. Revcolevschi, Neutron-diffraction study of the Jahn–Teller transition in stoichiometric $LaMnO_3$, Phys. Rev. B 57 (1998) R3189–R3192.

[10] Th. Proffen, R.G. DiFrancesco, S.J.L. Billinge, E.L. Brosha, G.H. Kwei, Measurement of the local Jahn–Teller distortion in $LaMnO_{3.006}$, Phys. Rev. B 60 (1999) 9973.

[11] X. Qiu, Th. Proffen, J.F. Mitchell, S.J.L. Billinge, Orbital correlations in the pseudocubic O and rhombohedral *R*-phases of $LaMnO_3$, Phys. Rev. Lett. 94 (2005) 177203.

[12] C.D. Ling, E. Grando, J.J. Neumeier, J.W. Lynn, D.N. Argyriou, Inhomogeneous magnetism in La-doped $CaMnO_3$: I, Mesoscopic phase separation due to lattice-coupled ferromagnetic interactions, Phys. Rev. B 68 (2003) 134439.

[13] T. Egami, S.J.L. Billinge, Underneath the Bragg Peaks: Structural Analysis of Complex Materials, Pergamon Press, Elsevier, Oxford, England, 2003.

[14] B.E. Warren, X-ray Diffraction, Dover, New York, 1990.

[15] P.F. Peterson, M. Gutmann, Th. Proffen, S.J.L. Billinge, PDFgetN: a user-friendly program to extract the total scattering structure function and the pair distribution function from neutron powder diffraction data, J. Appl. Crystallogr. 33 (2000) 1192.

[16] A.C. Larson, R.B. Von Dreele, General structure analysis system, Report No. LAUR-86-748, Los Alamos National Laboratory, Los Alamos, NM, 2000.

[17] B.H. Toby, Expgui, a graphical user interface for GSAS, J. Appl. Crystallogr. 34 (2001) 201–213.

[18] C.L. Farrow, P. Juhas, J.W. Liu, D. Bryndin, E.S. Božin, J. Bloch, Th. Proffen, S.J.L. Billinge, PDFfit2 and PDFgui: computer programs for studying nanostructure in crystals, J. Phys. Condens. Matter 19 (2007) 335219.

[19] A. Sartbaeva, S.A. Wells, M.F. Thorpe, E.S. Božin, S.J.L. Billinge, Quadrupolar ordering in $LaMnO_3$ revealed from scattering data and geometric modeling, Phys. Rev. Lett. 99 (2007) 155503.

[20] A. Sartbaeva, S.A. Wells, M.F. Thorpe, E.S. Božin, S.J.L. Billinge, Geometric simulation of perovskite frameworks with Jahn–Teller distortions: applications to the cubic manganites, Phys. Rev. Lett. 94 (2006) 065501.

[21] R.L. McGreevy, RMC: progress, problems and prospects, Nucl. Instrum. Methods Phys. Res. A 354 (1995) 1–16.

[22] S.A. Wells, M.T. Dove, M.G. Tucker, Finding best-fit polyhedral rotations with geometric algebra, J. Phys. Condens. Matter 14 (2002) 4567–4584.

[23] A. Sartbaeva, S.A. Wells, M.M.J. Treacy, M.F. Thorpe, The flexibility window in zeolites, Nat. Mater. 12 (2006) 962–965.

[24] I. Jeong, M.J. Graf, R.H. Heffner, Effects of Bragg peak profiles and nanoparticle sizes on the real-space pair distribution function, J. Appl. Crystallogr. 38 (2005) 55–61.

[25] R.D. Shannon, Revised effective ionic radii and systematic studies of interatomic potentials, Acta Cryst. A 32 (1976) 751.